Research in Astronomy and Astrophysics, 25:085001 (10pp), 2025 August https://doi.org/10.1088/1674-4527/addeb4
CSTR: 32081.14.RAA.addeb4

A Chandra X-ray Study of Dust Sputtering Model in the Cassiopeia A Supernova Remnant

Tianyi Lu[1,2], Xi Long[3], Wei Sun[1], Geng Chao[1,2], Zehao Jin[4], Hanzhang Feng[5], Min Long[6], and Li Ji[1]
[1] Key Laboratory of Dark Matter and Space Astronomy, Purple Mountain Observatory, Chinese Academy of Sciences, Nanjing 210008, China
[2] School of Astronomy and Space Science, University of Science and Technology of China, Hefei 230026, China
[3] Department of Physics, The University of Hong Kong, Pokfulam Road, Hong Kong, China; xilong@hku.hk
[4] Center for Astrophysics and Space Science (CASS), New York University Abu Dhabi, P.O. Box 129188, Abu Dhabi, UAE
[5] Department of Physics and Astronomy, Northwestern University, Evanston, IL 60208, USA
[6] Department of Computer Science, Boise State University, Boise, ID 83725, USA
Received 2025 May 7; revised 2025 May 25; accepted 2025 May 28; published 2025 June 17

Abstract

We use the Fe Kα emission in X-rays from non-equilibrium ionizing plasmas as a probe to explore the dust in supernova remnants (SNRs). We applied our model to Cassiopeia A (Cas A), a well-studied SNR with plenty of observational data as a test. We use Chandra Advanced CCD Imaging Spectrometer 980 ks data of Cas A, and AtomDB v3.0.9, an atomic database for X-ray plasma spectral modeling, to fit 248 spectra. A two-temperature model is adopted to describe the physical conditions of shocked ejecta and iron-rich plasma. We measure the Fe Kα flux ratio and the centroid difference of the dust and gas contributions. We find strong 6.4 keV line emission components, which indicates that iron-rich dust can survive within Cas A's shocked ejecta. We also find that the Fe Kα complex demonstrates an apparent double-hump structure in some Fe–K rich regions, which may be caused by both dust and multi-ejecta structure in Cas A. The results of Fe Kα structures are consistent with our model for a dust cloud embedded in multi-phase ejecta and suggest the presence of both dust sputtering and drag effects in those regions. It is currently still limited by the low spatial and spectrum resolution for the current X-ray detectors, but should be more useful when the new generation, high-resolution X-ray telescopes come into service.

Key words: (ISM:) dust, extinction – ISM: supernova remnants – shock waves – X-rays: ISM

1. Introduction

Dust is an essential component of the interstellar medium (ISM), playing a critical role in various processes at multiscales from star formation to galaxy evolution. A study on the formation, evolution, and composition of dust is a fundamental research area of ISM physics, but has not been fully understood. Dust was previously considered to be mainly produced by stellar winds from low-mass stars during their Asymptotic Giant Branch phase (Gehrz 1989). Later, the evidences of extinction features in the spectra of some high-redshift quasars reveal that dust grains existed in galaxies before a significant number of low-mass stars had evolved sufficiently to inject dust into the ISM (Pei et al. 1991; Dwek et al. 2007). Supernova (SN) explosions have been increasingly recognized as playing a vital role in producing and injecting dust into the ISM, especially in the early universe (Nozawa et al. 2003; Schneider et al. 2004; Cherchneff & Dwek 2010) for multiple reasons. First, elements such as C, Si, Ca, and Fe ejected by SN explosions could be crucial constituents of dust grains. Second, the dust production efficiency of SNe is considerable, with an average dust injection mass of $\gtrsim 1 M_{\odot}$ per SN in high-redshift galaxies (Dwek et al. 2007). It has also been shown that SNe in quasars and submillimeter galaxies at $z = 4$ collectively produced about $\sim 7 \times 10^7 M_{\odot}$ of dust within their host galaxies over approximately 2 Gyr (Rho et al. 2008).

The Fe Kα fluorescence emission line observed in the X-ray band can be a probe for investigating supernova remnant (SNR) dust. Strong Fe Kα lines are commonly detected in SNRs and play important roles in various aspects of SNR science, such as distinguishing progenitor types (Yamaguchi et al. 2014a; Siegel et al. 2021), and constraining the ionization age and electron temperature of the plasma (Yamaguchi et al. 2014b). Borkowski & Szymkowiak (1997) demonstrate that interstellar dust grains in hot plasmas can produce X-ray emission lines via fluorescence. Energetic electrons penetrating dust grains create inner-shell vacancies in atoms like iron, which then emit Kα photons (e.g., Fe Kα around 6.4 keV) in addition to the lines from collisional ionization. In addition to shifting the centroid, dust produces a characteristic line profile shape. The neutral Fe Kα photons from dust appear as an "asymmetric, redshifted shoulder" on the low-energy side of the overall Fe Kα line. In other words, the Fe Kα complex in a dusty plasma should be skewed, with an extended low-energy wing due to the 6.4 keV component. This effect would be especially noticeable when the dust line is well-separated in energy from the ionized Fe lines (e.g., in a plasma where most Fe is He-like/H-like, ∼6.7 keV). Such a red wing in the Fe Kα profile is an important observational clue: its presence would strongly indicate fluorescent Fe emission from dust grains. Borkowski & Szymkowiak (1997) conclude that fluorescent Fe Kα lines from dust likely occur in young SNRs' spectra, meaning that one cannot successfully model the X-ray lines without accounting for iron depleted into dust and its fluorescent emission. Incorporating these effects not only improves spectral fits but also provides a novel way to gauge the amount of iron residing in dust grains in objects like Cassiopeia A (Cas A) by comparing the dust-origin Fe Kα emission to that from ionized iron. Low-energy cosmic rays (CRs)—e.g., keV electrons or MeV protons—can ionize the Fe K-shell in neutral or weakly ionized gas, producing 6.4 keV Kα lines (Tatischeff et al. 2012; Saji et al. 2018; Nobukawa et al. 2019). In Cas A, the fast shocks can accelerate particles, and if those CRs encounter Fe-rich ejecta or clumps they could yield 6.4 keV. However, there is no firm evidence that Cas A is interacting with dense gas (Zhou et al. 2018), so the target for CRs would be the ejecta itself in gas or dust form.

Cas A, a ∼350 yr old core-collapse SNR (Fesen et al. 2006), provides an especially compelling case for this phenomenon. The observed Fe Kα feature in Cas A appears to have a slight asymmetry or tail toward lower energies that cannot be explained by ionized Fe emission alone. This is motivation to search for a 6.4 keV fluorescent line that emerges underneath the dominant 6.6–6.7 keV line. Cas A also contains substantial dust (detected via its infrared thermal emission), so it is plausible that some fraction of its Fe remains in grain form and produces this fluorescent Kα component. The implication is that the ionization timescale of Cas A's Fe-rich plasma might be even higher than one would infer without dust, since a small 6.4 keV contribution can make the centroid appear slightly lower (younger) than the true state. More generally, the Cas A data reinforce that fluorescent Fe Kα lines from dust are likely present in young SNRs and should be considered when interpreting their spectra. Ignoring dust can lead to inaccurate modeling of Fe lines, whereas including a dust-origin 6.4 keV component can improve fits and yield more physically realistic parameters (e.g., higher τ for Cas A's shocked ejecta). Cas A's Fe Kα characteristics—a high 6.6 keV centroid with a faint red wing (Borkowski & Szymkowiak 1997)—are consistent with a mostly ionized plasma that still harbors a minor but detectable contribution from Fe in dust grains.

In this study, we aim to use Chandra's high spatial resolution to conduct a region-by-region spectral search for significant 6.4 keV emission. By isolating specific areas within Cas A that may contain relatively unprocessed ejecta or enhanced dust content, we can better assess the spatial distribution of neutral Fe fluorescence and identify sites where dust grains may still survive and contribute to the X-ray spectrum. We present a spectral analysis of Fe–K rich regions in Cas A. We use an empirical model of power-law of for continuum to detect emissions at 6.4 keV. The regions showing significant 6.4 keV emission were further analyzed using a two-temperature plasma model to identify evidence of emission from dust. This paper is organized as follows: we briefly describe the data of Chandra Advanced CCD Imaging Spectrometer (ACIS) observations of Cas A and data reduction methods in Section 2; present the results of our spectral fits using the empirical model and the two-temperature plasma models in Section 3; and provide a summary and conclusion in Sections 4 and 5.

Table 1
Observation Information

Obs ID	Instrument	Start Date	Exposure (ks)	PI Name[a]
4634	ACIS-S	2004-04-28 05:43:26	148.62	Hwang
4635	ACIS-S	2004-05-01 00:44:20	135.04	Hwang
4636	ACIS-S	2004-04-20 08:41:03	143.48	Hwang
4637	ACIS-S	2004-04-22 18:22:53	163.50	Hwang
4638	ACIS-S	2004-04-14 19:47:55	164.53	Hwang
4639	ACIS-S	2004-04-25 09:37:41	079.05	Hwang
5196	ACIS-S	2004-02-08 17:41:35	049.52	Hwang
5319	ACIS-S	2004-04-18 21:18:33	042.26	Hwang
5320	ACIS-S	2004-05-05 22:59:36	054.37	Hwang
Total			980.37	

Note.
[a] PI Name refers to the Principal Investigator of each observation.

2. Data and Data Reduction

We use the 980 ks ACIS observation obtained by the Chandra X-ray Observatory in 2004, detected by the ACIS-S3 detector, which contains nine observation segments, observed by Hwang & Laming (2003) and Laming & Hwang (2003). We list the observation information in Table 1. We select observations having as many segments as possible within the same year to reduce fitting errors and improve the S/N.

The software we used includes: Chandra Interactive Analysis of Observation (version 4.14, with the CALDB version 4.9.6) for data analysis; XSPEC (version 12.12.0, Arnaud 1996; with AtomDB v3.0.9; Smith et al. 2001; Foster et al. 2012) for fit spectrum. Here, the *cstat* is selected as the fitting statistic. In addition, we fit the source and background spectra simultaneously in XSPEC, instead of subtracting the background spectra. The spectra are rebinned and grouped for plotting purposes.

3. Spectral Analysis

We divided Fe–K rich regions in Cas A (DeLaney et al. 2010) into directional sectors and radial shells as shown in

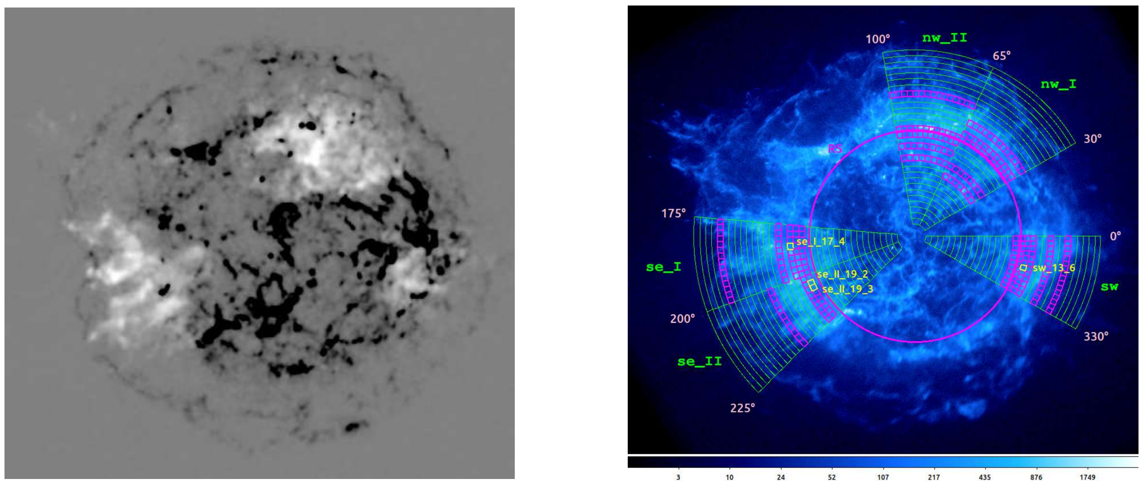

(a) (b)

Figure 1. (a) Spectral tomographic image of the Fe K emission as positive brightness (DeLaney et al. 2010). The light area represents strong Fe K emission (6–7 keV) relative to the continuum emission (4–6 keV). (b) The radial pie shell spectrum extraction regions marked on a normal Chandra ACIS-S image (0.1–10.0 keV) with nw_I, nw_II, se_I, se_II, sw corresponding to five big pie sections. Each section is split into several small shells. The purple circle marked out the current location of the RS in Cas A (Orlando et al. 2022). The small purple grids split the dusty shell radially. The yellow grids denote the dusty cells for which the extracted example spectrum is shown in Figure 4.

Figure 1. To search for dust emission, we apply a two-step analysis of the spectra. First, we fit the spectra with an empirical method to identify the region with a significant 6.4 keV neutral Fe line. The empirical model comprises a power-law for the continuum and three Gaussian emission lines. The Gaussian line fixed at 6.4 keV (representing the neutral iron Kα line from dust) had zero intrinsic width, while the other two lines represent iron Kα and Kβ (or a blend of iron Kβ and nickel Kα) from shocked gas, with free centroid energies and widths. Shells with significant 6.4 keV Fe line detection, which has the flux ratio $R_d = f_{6.4}/f_{\rm gas}$ deviating from 0 at 3σ significance level, were further divided into smaller boxes ($5'' \times 5''$), $f_{6.4}$ is the flux of the first Gaussian line representing the neutral iron Kα line, $f_{\rm gas}$ is the second Gaussian line which is the collisional ionized Fe kα component. Each spectrum (0.5–8 keV) from the box region was fitted using a physical two-temperature non-equilibrium ionizing (NEI) plasma model (*tbabs*(*vpshock* + *vnei*)), with abundances and redshifts free. Finally, a Gaussian line, representing emission from the dust, was added, and correlations between its centroid energy and plasma redshift were analyzed.

3.1. Empirical Model

Spectra from each shell were extracted in the Fe–K band (5.0–8.0 keV) and fitted with an empirical model composed of a power-law continuum plus three Gaussian lines. The first Gaussian component (*gau1*), representing neutral Fe Kα emission from dust, was fixed at 6.4 keV with zero intrinsic width. The second and third Gaussian components (*gau2* and *gau3*), accounting for the Fe Kα and Fe Kβ (or a mixture of Fe Kβ and Ni Kα) emission from shocked ejecta or ISM, had freely varying centroid energies, widths, and normalizations.

We calculated the flux ratio *gau1* to *gau2*, $R_d \equiv f_{6.4}/f_{\rm gas}$, for each shell and selected those with dust emission above a 3σ significance threshold for further analysis in Section 3.2. The radial profiles of the gau2 centroid and R_d for each sector from the empirical model fitting are shown in Figure 3. An increase in the centroid energy near the reverse shock (RS) reflects the recent RS interaction and heating of Fe-rich ejecta. Each sector contains about five shells meeting the 3σ threshold, identifying them as potential regions where dust has survived. Spectra from these dust-rich shells typically show either a red wing at Fe Kα, consistent with the scenario described by Borkowski & Szymkowiak (1997), or a distinct hump near 6.4 keV if the gas emission centroid energy is sufficiently high. An example spectrum from one of these Fe–K-rich dusty shells is presented in Figure 2.

3.2. Physical Model

Shells selected from the empirical model fitting were subdivided into $5'' \times 5''$ box regions. The box size was chosen to ensure sufficient photon statistics while minimizing contamination from plasma components with varying temperatures and ionization states. We then fitted the extracted spectra from these box regions using a physically motivated model. Given that the plasma in Cas A is in an NEI state (Hwang & Laming 2012; Rutherford et al. 2013), we fit the spectra in 0.5–8.0 keV with an absorbed two-temperature plasma model *tbabs*(*vpshock* + *vnei*). The low-temperature

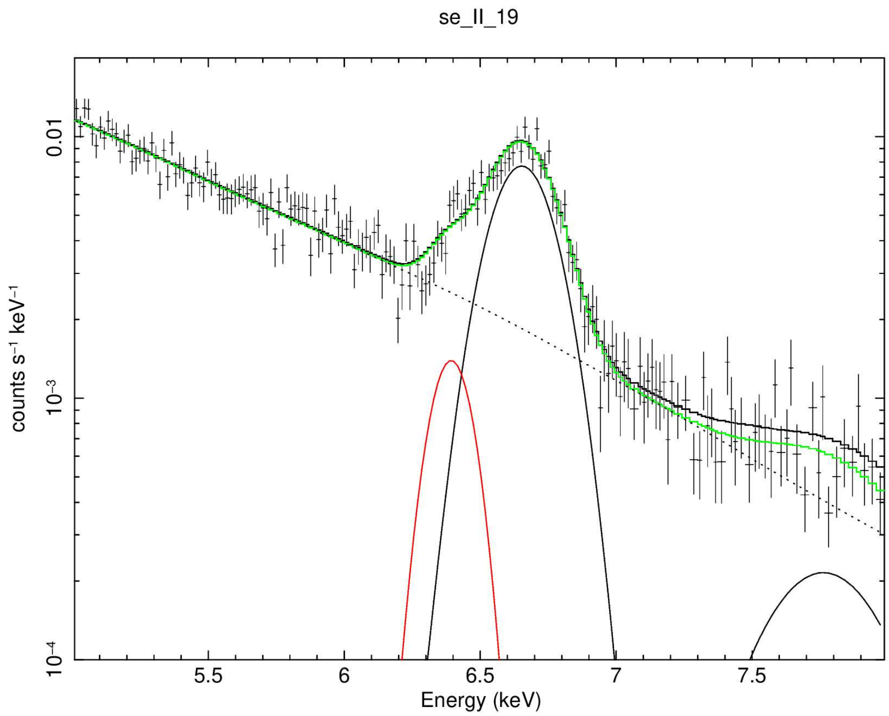

Figure 2. Example spectrum which contains Fe Kα red wing feature from our pie regions: best fit result from the 19th shell (from the outermost to inside) in sector se_II. Data points have been rebinned for a significance of 3σ on every 15 counts in plotting. The green is the source spectrum, and the black one is the total flux curve. Three Gaussian hump components are gau1, gau2, gau3 from left to right, respectively. Red hump (gau1) is regarded as the dust component. Black humps (gau2, gau3) near 6.6 and 7.8 keV correspond to the Fe Kα and Fe Kβ complex contributed by gas (maybe Fe Kβ is a mixture signal of Fe Kβ and Ni Kα), respectively.

component *vpshock* represents shocked, iron-poor NEI material, while the high-temperature component *vnei* describes the hot, iron-rich NEI plasma. A similar modeling approach was previously applied to spectra from iron-rich ejecta regions (Hwang & Laming 2009, 2012). We used the solar abundances from Wilms et al. (2000).

For *vpshock*, abundances of O, Ne, Mg, Si, S, Ar, Ca, and Fe were allowed to vary freely, while only Fe abundance was free in the *vnei* component. Given the radial velocities of $\sim 10^3\ \mathrm{km\,s^{-1}}$ according to Hwang et al. (2001), DeLaney et al. (2010), the redshift parameter of each component was allowed to vary during fitting.

After obtaining the best fit result from the model *tbabs* (*vpshock*+*vnei*), we introduced an additional Gaussian line to model possible dust emission. The energy of the Gaussian line was initially set to 6.4 keV and allowed to vary, with its intrinsic width fixed at zero and normalization free. After fitting the full dataset, we examined the correlation between the fitted Gaussian line centroid energy (lineE) and the redshift of the high-temperature component.

In our two-temperature model fitting, most box regions yielded reduced $\chi^2 < 1.3$. However, several regions exhibited relatively poor fits, with reduced $\chi^2 \gtrsim 1.5$. These regions shared a common feature of significantly higher brightness compared to others, indicating more complex temperature structures. This finding is consistent with results reported by Hwang & Laming (2012), the reduced χ^2 map (first subfigure in their Figure 1) similarly shows small, bright regions with large reduced χ^2 (about 2–9), and their spatial distributions are highly consistent with bright regions. Additionally, some of these bright regions displayed strong Ti–K or Cr–K emission, resulting in large residuals (up to 5 σ) near the Ti Kα or Cr Kα lines.

Spectral analysis revealed that the lower-energy band ($\lesssim$4 keV) is predominantly described by the vpshock component *vpshock*, whereas the *vnei* component contributes mainly at higher energies ($\gtrsim$4 keV). Comparison of fitting results before and after adding the Gaussian component indicated no significant changes in the derived parameters, kT_e, τ, normalization of *vnei* component, unless the parameter cannot be well restricted.

3.2.1. Fe Kα Feature

As shown in Figure 4, features near the lower energy end of Fe Kα complexes appear more distinctly in some individual cells compared to the shell spectra they belong to, exhibiting three main characteristics in the extracted spectra. The first feature is an overly broad Fe Kα complex, which cannot be

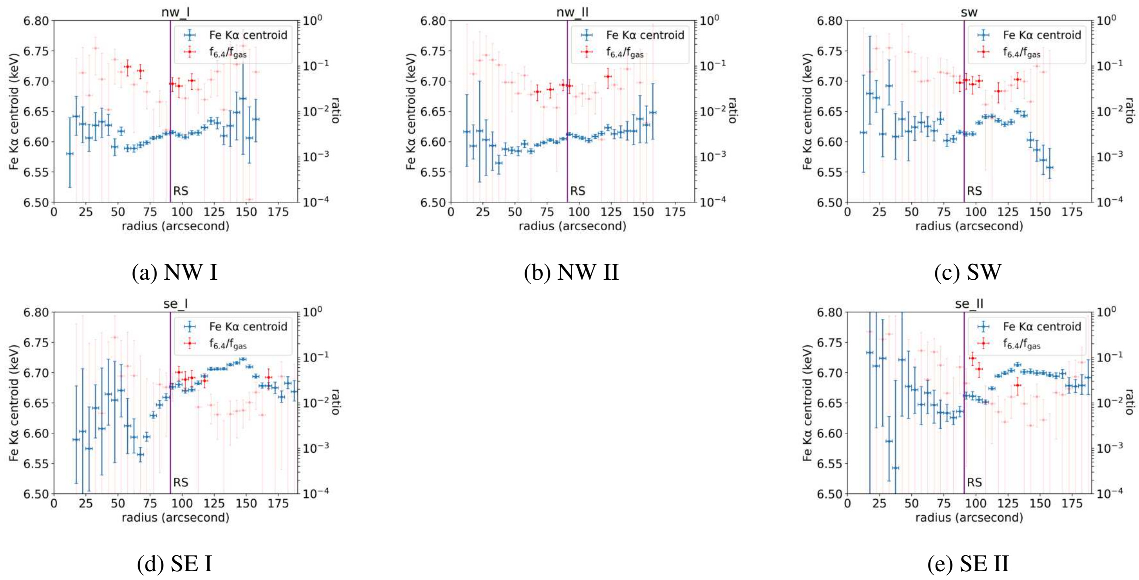

(a) NW I (b) NW II (c) SW

(d) SE I (e) SE II

Figure 3. The gau2 centroid and profile of R_d at five pie regions in the empirical model. Faint red points mark R_d values with $<3\sigma$ significance in fitting. All error bars show the 90% confidence range. The purple vertical line marks the current RS radius.

fully described by the *vnei* model alone. The second feature is a distinct plateau or "platform" at the lower energy edge of the Fe Kα complex, indicating that the flux density decreases more slowly toward the lower energy end, whereas the higher energy end declines more sharply. The third feature manifests as a double-humped structure separated by a gap of approximately 200–300 eV hump gap. Collectively, these features suggest the presence of an additional ionization component characterized by a lower ionization age in Fe ejecta across numerous dusty cells. We provide the spectral fitting results in Tables 2 and 3 for the regions in Figure 4. Our results are largely consistent with previous studies. For instance, the velocity range of Fe ejecta derived from our analysis is within ± 4000 km s^{-1}, which agrees with earlier observations and 3D Doppler reconstructions (DeLaney et al. 2010; Milisavljevic & Fesen 2013). Additionally, the derived ionization ages for the vpshock component fall within the range of 10^{11}–10^{12} cm^{-3}s, consistent with values reported by Hwang & Laming (2012).

We generated distribution diagrams showing the relationship between lineE (6.4) and the redshift of the *vnei* component. Cells were filtered based on several customized conditions relevant to the fitting scenario. The first constraint was the component significance, requiring the 6.4 keV component to exceed a statistical significance of 3σ. This was the most important constraint. The second constraint involved the centroid energy lineE(6.4). Due to its freedom during fitting, in some cells the best fit value exceeded the centroid of the Fe Kα emission from the *vnei* component, a scenario that cannot be explained by our dust model. We empirically filtered out cells where the fitted lineE(6.4) was greater than 6.55 keV. The third constraint concerned normalization, specifically ensuring the ratio of the normalization of *vpshock* component to that of the *vnei* component should be no less than $1/10$. Otherwise, spectra from these cells would unphysically show a minor *vpshock* contribution and a disproportionately large *vnei* contribution to the Fe Kα band. After applying these constraints, 121 spectra remained.

An anti-correlation between lineE(6.4) and the *vnei* redshift is apparent in each pie region, and even within some shell groups, particularly in the NW and SW regions as shown in Figure 5. Although a global anti-correlation in the SE sector is less evident, it is locally clear, for example, in three cells from sector SE_II. These results support the dust drag effect hypothesis. After the explosion, dust embedded in shocked gas is forced to co-move with the gas, as suggested by trajectory and dynamical analyses of shocked dust by Nozawa et al. (2006). This process leads to an additional dust sputtering mechanism known as non-thermal sputtering. We calculated the timescale for non-thermal sputtering (as well as dust deceleration due to drag) in Cas A using the method described by Nozawa et al. (2006) and found that it is shorter than the age of the remnant.

4. Discussion

Iron dust observed in the X-ray band is used to trace dust enclosed by hot ejecta ($>10^6$ K) in SNR, as well as the clumps and diffuse X-ray gas surrounding them. The positions of the dusty cells marked in Figure 1 are well consistent with the dusty regions observed in infrared in previous works (De Looze et al. 2017; Niculescu-Duvaz et al. 2021), especially in

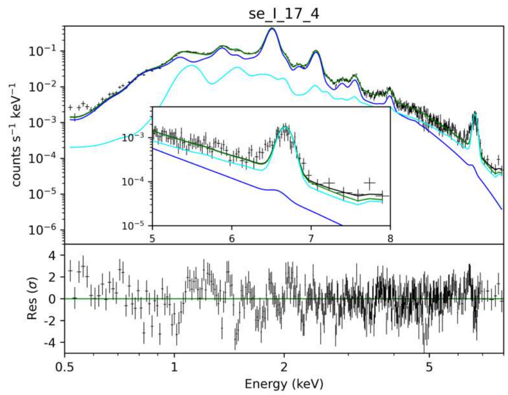

(a) SE_I_17_4 region

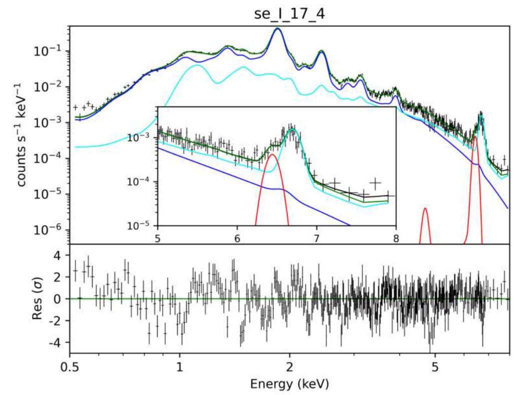

(b) SE_I_17_4 region with zgauss

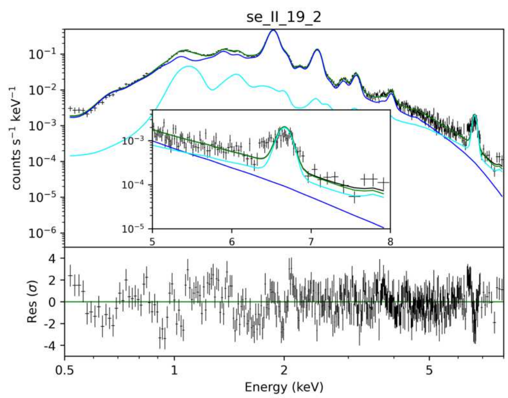

(c) SE_II_19_2 region

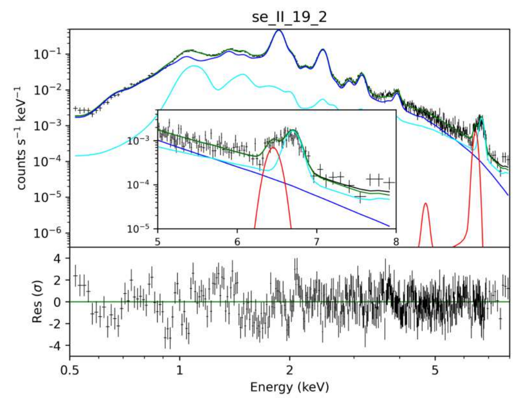

(d) SE_II_19_2 region with zgauss

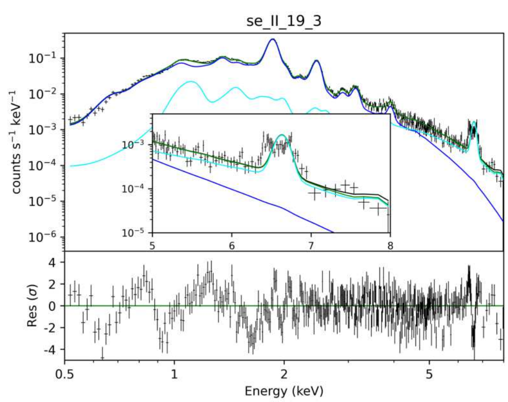

(e) SE_II_19_3 region

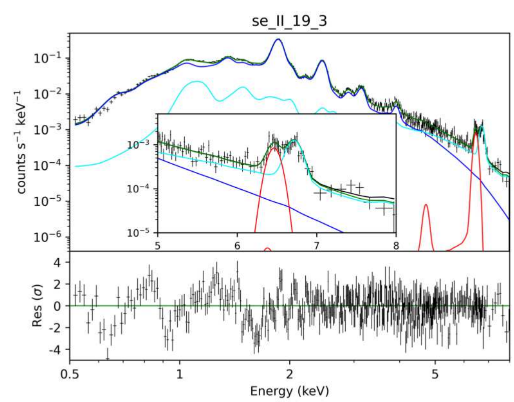

(f) SE_II_19_3 region with zgauss

Figure 4. Example spectra showing Fe Kα emission with two apparent ionization components. Data points are rebinned for 3σ significance every 15 counts. Dark blue lines show the *vpshock* component, light blue the *vnei* component, and red the *zgauss* component. Black and green lines are the fitted total and source spectra, respectively. Insets zoom in on the Fe–K band, highlighting the Fe Kα complex structure.

sector SE_II. A large amount of cold dust($<10^2$ K) can be found in the southeast of the SNR image from the infrared band, as well as in the northwest and southwest regions. This indicates that these low-ionization Fe Kα components can be produced by dust embedded in hot gas. It also indicates that the ejecta and clumps in these regions are multi-phase, consistent with previous conclusions (Rho et al. 2019).

After being swept by the RS, it is difficult for dust to survive in diffuse X-ray gas. The enormous power and high dust destruction efficiency of the RS in Cas A can destroy 92%–

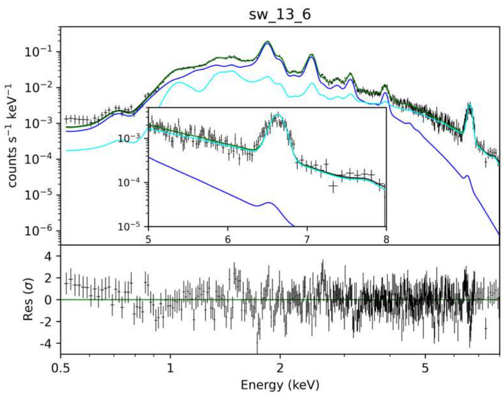

(g) SW_13_6 region

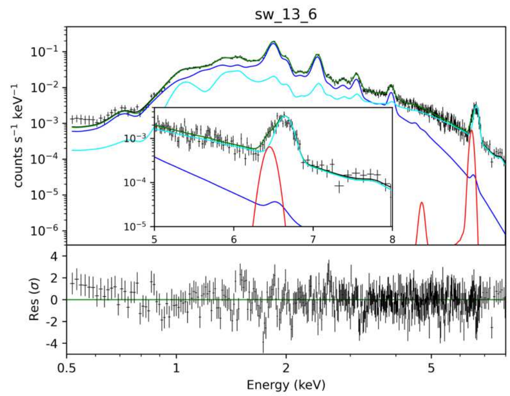

(h) SW_13_6 region with zgauss

Figure 4. (Continued.)

98% of dust near the shock (Priestley et al. 2022). Therefore, the dust-to-gas mass ratio ($\lesssim 10^{-3}$) in X-rays will be much lower than in the pre-shock gas, post-shock gas, and clumps (Priestley et al. 2019, 2022). However, estimates from Nath et al. (2008) and Micelotta et al. (2016) indicate that only 1%–20% of dust grains will be sputtered in the SNR ejecta. They also suggest that dust cooling is effective in metal-rich ejecta.

Our dust sputtering model assumes a power-law distribution for dust grain radius (Mathis et al. 1977, hereafter MRN). However, this assumption is a simple and natural mathematical model since it is currently impossible to observationally verify the real-time radius distribution of SNR dust grains. Another widely accepted hypothetical distribution is the log-normal distribution, which has been applied in studies of dust and its interaction with shocks in Cas A (Kirchschlager et al. 2019, 2020; Slavin et al. 2020; Niculescu-Duvaz et al. 2021). If we adopt an initial grain radius distribution as a log-normal, the dust sputtering rate function with respect to τ will change. However, we predict that this will only slightly impact the MRN-based model, because as time progresses, the distribution will rapidly become dominated by a power-law, accompanied by a weak log-normal component (Kirchschlager et al. 2019). Furthermore, the smaller the initial peak radius of the log-normal, the lower the relative proportion of the log-normal component in the final distribution. The power-law distribution itself does not transform into another type of distribution over time. Naturally, this is simply one possible way to improve our dust model; it does not imply that the MRN distribution is incorrect in this scenario. Indeed, MRN has also been widely used in dust studies of Cas A (De Looze et al. 2017; Priestley et al. 2019, 2022).

One possible explanation for the additional Fe ejecta component manifested from the Fe Kα structure is a two-redshift mixed ejecta. The first two features we mentioned in Section 3.2.1 both consist of a main component accompanied by a relatively weak component at the red wing. Without additional factors, the intensities of these two components should not systematically appear as a strong-weak intensity pair, as described above. Thus, this explanation might only account for the double-hump structure. The gap between the two humps varies from about 200–300 eV in spectra exhibiting this feature (see Figure 4), while the Fe Kα complex centroid typically ranges from approximately 6400 to 6700 eV. If we include the Fe XXVI Lyα line in the complex, the upper limit of the centroid increases to about 6800 eV. The Doppler velocity difference depends on $\Delta E/E$. If we choose the lower limit of its possible value range, 200/6800, this corresponds to a velocity difference of $\sim$8800 km s^{-1}. This implies that if these line gaps entirely result from two redshifted components, the minimum velocity difference should be $\gtrsim$9000 km s^{-1}. However, if we separate the radii shown in Figure 10 from DeLaney et al. (2010) into several discrete bins with widths of 5″, we find the maximum velocity difference among the three main blocks of Fe–K rich regions is $\sim$4000 km s^{-1} across all 5″ radial bins. Additionally, since each spectrum extraction region is restricted within a 5″ × 5″ box, only a portion of points from each radius bin in Figure 10 (DeLaney et al. 2010) is included in our analysis. This indicates that the velocity difference described above is certainly less than 4000 km s^{-1}, meaning that the actual line centroid gap is less than 100 eV. This gap is smaller than half of the centroid gap observed in our spectra and is challenging to resolve clearly with Chandra ACIS-S3.

The lower-energy Fe Kα line, the Gaussian line component in our spectral model and the Kα emission from iron-high ejecta, have an energy gap of 200–300 eV. Based on the dust sputtering model (Borkowski & Szymkowiak 1997), which thermal sputtering by hot plasma erodes dust grains and releases refractory elements such as Fe into the gas phase, we find that the Fe Kα centroid shift is about 150–250 eV when τ is $\sim 10^{11}$ cm^{-3} s and kT_e is 2–10 keV. This result aligns well

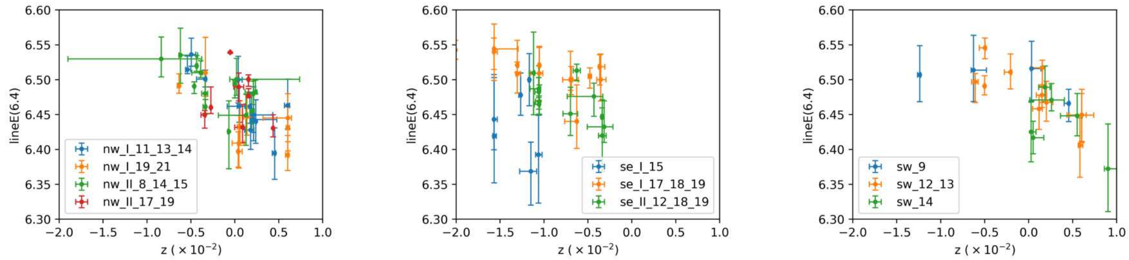

(a) NW region (b) SE region (c) SW region

Figure 5. Scatter plots showing the relationship between the fitted line energy of Fe Kα (6.4 keV) and the redshift of the high-temperature spectral component in extraction cells from five pie regions. All error bars represent the 90% confidence intervals. Legend labels follow the format: `[pie]_[shell1]_[shell2]`.

Table 2
Examples of Spectral Fitting Results Before and After Adding the Dust Line (I)

Component	Parameter	se_I_17_4		sw_13_6	
		No Dust Line	With Dust Line	No Dust Line	With Dust Line
tbabs	$N_{\rm H}$ (10^{22} cm^{-2})	$1.53^{+0.03}_{-0.01}$	$1.49^{+0.01}_{-0.02}$	3.22 ± 0.03	$3.20^{+0.07}_{-0.03}$
	kT_e (keV)	$1.34^{+0.02}_{-0.03}$	$1.42^{+0.02}_{-0.05}$	$0.83^{+0.01}_{-0.03}$	$0.87^{+0.03}_{-0.00}$
(*vpshock*)	[O]	$1.35^{+0.23}_{-0.08}$	1.23 ± 0.07	$1.42^{+0.31}_{-0.35}$	$0.72^{+0.58}_{-0.41}$
	[Ne]	$0.73^{+0.08}_{-0.09}$	0.72 ± 0.04	$0.82^{+0.52}_{-0.40}$	$0.94^{+0.48}_{-0.34}$
	[Mg]	$0.96^{+0.02}_{-0.03}$	$1.01^{+0.03}_{-0.02}$	$0.47^{+0.06}_{-0.08}$	$0.52^{+0.11}_{-0.05}$
	[Si]	$6.41^{+0.40}_{-0.32}$	6.72 ± 0.08	$3.04^{+0.09}_{-0.06}$	$2.84^{+0.12}_{-0.25}$
	[S]	$4.57^{+0.08}_{-0.14}$	$4.72^{+0.12}_{-0.09}$	$2.83^{+0.22}_{-0.07}$	$2.64^{+0.12}_{-0.13}$
	[Ar]	4.84 ± 0.37	$4.88^{+0.40}_{-0.36}$	$4.34^{+0.73}_{-0.32}$	3.91 ± 0.29
	[Ca]	$7.99^{+0.99}_{-0.93}$	$8.05^{+1.06}_{-0.88}$	$8.13^{+0.84}_{-0.82}$	$7.19^{+0.73}_{-0.74}$
	[Fe]	$0.01^{+0.02}_{-0.01}$	$0.00^{+0.02}_{-0.00}$	$1.14^{+0.21}_{-0.11}$	1.16 ± 0.06
	τ_u (10^{11} cm^{-3} s)	$1.49^{+0.11}_{-0.06}$	$1.34^{+0.06}_{-0.04}$	$56.46^{+20.21}_{-22.34}$	$18.52^{+7.24}_{-1.67}$
	redshift (10^{-3})	$-8.02^{+0.04}_{-0.00}$	$-8.02^{+0.04}_{-0.00}$	$-3.40^{+0.22}_{-0.36}$	$-3.40^{+0.24}_{-0.22}$
	norm[a] (10^{-4})	$13.30^{+0.05}_{-0.14}$	$11.98^{+0.12}_{-0.76}$	$38.00^{+0.55}_{-1.00}$	$37.20^{+0.44}_{-3.22}$
Fe ejecta	kT_e (keV)	$2.83^{+0.27}_{-0.07}$	$2.41^{+0.05}_{-0.08}$	$6.13^{+0.37}_{-0.28}$	$5.86^{+0.46}_{-0.34}$
(*vnei*)	[Fe]	$2.82^{+0.14}_{-0.11}$	$2.64^{+0.13}_{-0.19}$	$4.62^{+0.32}_{-0.41}$	$3.68^{+0.42}_{-0.31}$
	τ (10^{11} cm^{-3} s)	$2.55^{+0.08}_{-0.20}$	$3.42^{+0.30}_{-0.37}$	$0.50^{+0.01}_{-0.02}$	$0.58^{+0.05}_{-0.04}$
	redshift (10^{-3})	$-3.36^{+0.12}_{-0.26}$	$-6.99^{+0.89}_{-0.90}$	$-5.02^{+0.10}_{-0.09}$	$-6.08^{+0.32}_{-0.41}$
	norm[a] (10^{-4})	$2.89^{+0.15}_{-0.07}$	$3.32^{+0.10}_{-0.16}$	3.36 ± 0.16	$3.33^{+0.32}_{-0.41}$
dust line	lineE (keV)	…	$6.500^{+0.041}_{-0.015}$	…	$6.497^{+0.012}_{-0.030}$
(*gauss*)	norm (10^{-7})	…	$7.96^{+1.44}_{-2.20}$	…	$12.08^{+3.71}_{-2.48}$
χ^2/d.o.f.		1.172	1.165	1.114	1.111

Note.
[a] Normalization is defined as: $(10^{-14}/[4\pi D_A^2(1+z)^2])\int n_e n_{\rm H} dV$, where D_A is the angular diameter distance to the source (cm), and n_e, $n_{\rm H}$ are electron and hydrogen number densities (cm^{-3}).

with our spectral fitting results, especially the observed centroid gap range of the two hump structures of Fe Kα complex. This consistency provides a reason to consider dust-originated Fe Kα as a plausible explanation for this additional ionization component. Otherwise, alternative mechanisms must be explored to explain the low-ionization states of Fe. Bamba et al. (2025) also observed and found that Fe Kα line profile is highly asymmetric, with a clear low-energy tail and blending of multiple lines from XRISM/Resolve data. This blending cannot be treated as a single line for Doppler measurements. This asymmetry is a clear spectral signature of incomplete ionization; some fraction of the Fe remains at lower charge states, emitting slightly lower-energy Kα line and thus skewing the complex line shape. Although a larger

Table 3
Examples of Spectral Fitting Results Before and After Adding the Dust Line (II)

Component	Parameter	se_II_19_2		se_II_19_3	
		No Dust Line	With Dust Line	No Dust Line	With Dust Line
tbabs	N_H (10^{22} cm^{-2})	1.05 ± 0.01	$1.04^{+0.01}_{-0.02}$	1.80 ± 0.01	1.78 ± 0.01
	kT_e (keV)	$1.63^{+0.05}_{-0.02}$	$1.69^{+0.11}_{-0.05}$	0.94 ± 0.01	1.00 ± 0.04
(*vpshock*)	[O]	$0.00^{+0.02}_{-0.00}$	0.00 ± 0.00	$17.05^{+6.02}_{-0.64}$	$22.96^{+0.79}_{-0.91}$
	[Ne]	$0.12^{+0.05}_{-0.02}$	0.12 ± 0.04	$3.33^{+1.09}_{-0.10}$	$5.11^{+0.17}_{-0.15}$
	[Mg]	$0.52^{+0.03}_{-0.02}$	$0.53^{+0.02}_{-0.03}$	$2.13^{+0.08}_{-0.07}$	$3.52^{+0.12}_{-0.10}$
	[Si]	$5.80^{+0.27}_{-0.12}$	$5.81^{+0.27}_{-0.14}$	$15.56^{+0.19}_{-0.17}$	$22.73^{+9.01}_{-0.29}$
	[S]	$4.92^{+0.31}_{-0.08}$	$4.90^{+0.09}_{-0.12}$	$12.61^{+0.25}_{-3.56}$	$17.84^{+7.20}_{-0.38}$
	[Ar]	$5.72^{+0.32}_{-0.30}$	$5.66^{+0.30}_{-0.29}$	$14.09^{+1.15}_{-1.14}$	$19.17^{+1.65}_{-1.57}$
	[Ca]	$5.83^{+0.58}_{-0.54}$	$5.84^{+0.55}_{-0.52}$	$19.31^{+2.99}_{-3.18}$	$26.25^{+4.35}_{-4.20}$
	[Fe]	0.00 ± 0.00	0.00 ± 0.00	$0.59^{+0.19}_{-0.04}$	$0.75^{+0.07}_{-0.10}$
	τ_u (10^{11} cm^{-3} s)	$1.70^{+0.09}_{-0.06}$	$1.60^{+0.12}_{-0.14}$	$3.87^{+0.39}_{-0.11}$	3.13 ± 0.07
	redshift (10^{-3})	$-13.35^{+0.04}_{-0.05}$	$-13.31^{+0.01}_{-0.09}$	$-11.80^{+0.02}_{-0.01}$	$-11.79^{+0.04}_{-0.01}$
	norm[a] (10^{-4})	$14.40^{+0.45}_{-0.49}$	$13.99^{+0.57}_{-0.51}$	$7.40^{+0.04}_{-0.30}$	$4.67^{+1.67}_{-0.03}$
Fe ejecta	kT_e (keV)	$10.00^{+\infty}_{-1.37}$	$10.00^{+\infty}_{-1.63}$	$5.30^{+0.25}_{-0.40}$	$3.12^{+0.08}_{-0.06}$
(*vnei*)	[Fe]	$3.23^{+0.41}_{-0.40}$	$3.46^{+0.69}_{-0.30}$	$3.33^{+0.19}_{-0.14}$	2.84 ± 0.14
	τ (10^{11} cm^{-3} s)	$0.67^{+0.03}_{-0.02}$	0.63 ± 0.03	$0.97^{+0.05}_{-0.03}$	$1.68^{+0.07}_{-0.21}$
	redshift (10^{-3})	$-3.54^{+0.22}_{-0.26}$	$-10.54^{+0.01}_{-0.44}$	$-3.40^{+0.10}_{-1.19}$	$-10.57^{+0.11}_{-0.55}$
	norm[a] (10^{-4})	$1.14^{+0.12}_{-0.10}$	$0.97^{+0.10}_{-0.18}$	1.80 ± 0.15	$2.73^{+0.08}_{-0.07}$
dust line	lineE (keV)	⋯	$6.469^{+0.024}_{-0.019}$	⋯	$6.465^{+0.012}_{-0.014}$
(*gauss*)	norm (10^{-7})	⋯	$10.30^{+2.49}_{-2.25}$	⋯	$14.51^{+2.16}_{-2.22}$
χ^2/d.o.f.		1.156	1.144	1.205	1.184

Note.
[a] Table notes are the same as in Table 2.

extraction region, 30″ × 30″, could include plasma with a range of temperatures and ionization ages, we restrict our spectral extraction to a smaller region, 5″ × 5″, to minimize contamination by multiple components. With its anticipated spectral resolution of 2.5 eV up to 7 keV and spatial resolution of ∼ 5″ (in-focus at 1 keV) provided by the X-IFU instrument, Advanced Telescope for High-ENergy Astrophysics (Athena; Barret et al. 2023) will enable precise separation of the 6.4 keV Fe Kα fluorescence line from neutral or low-ionization iron and the adjacent lines from He-like and H-like Fe. This capability will facilitate the direct detection of dust-originated Kα emission.

5. Conclusion

We present a Chandra 980 ks exposure analysis of the Galactic SNR Cas A. This is a new attempt for the connection of SNR dust model to X-ray observations. Our analysis supports the presence of neutral or low-ionization Fe Kα emission likely associated with dust surviving in the hot, metal-rich ejecta of Cas A. We discover a low-ionization component in Fe ejecta by Fe Kα line analysis from Chandra ACIS-S3 X-ray spectra in Cas A, which is possibly contributed from Fe atoms locked in the dust. The observed double-hump structures in the Fe Kα line profile cannot be fully explained by Doppler shifts from redshifted or mixed-ionization ejecta alone. Instead, the centroid gap between components aligns well with theoretical predictions of dust-origin Fe Kα emission, providing compelling evidence that dust contributes to the spectral complexity. These results highlight the need to incorporate dust into spectral models of Cas A and similar SNRs. Athena's X-IFU will enable precise separation of the 6.4 keV Fe Kα fluorescence line from neutral or low-ionization Fe and nearby lines, enabling direct detection of Kα emission originating from dust.

Acknowledgments

We are grateful to the referee for their insightful comments and constructive suggestions, which helped improve the manuscript. X.L. is supported by a GRF grant of the Hong Kong Government under HKU 17304524.

ORCID iDs

Xi Long https://orcid.org/0000-0003-3350-1832
Wei Sun https://orcid.org/0000-0002-5456-0447

References

Arnaud, K. A. 1996, in ASP Conf. Ser. 101, Astronomical Data Analysis Software and Systems V, ed. G. H. Jacoby & J. Barnes (San Francisco, CA: ASP), 17
Bamba, A., Agarwal, M., Vink, J., et al. 2025, PASJ, psaf041
Barret, D., Albouys, V., Herder, J.-W. d., et al. 2023, ExA, 55, 373
Borkowski, K. J., & Szymkowiak, A. E. 1997, ApJL, 477, L49
Cherchneff, I., & Dwek, E. 2010, ApJ, 713, 1
De Looze, I., Barlow, M. J., Swinyard, B. M., et al. 2017, MNRAS, 465, 3309
DeLaney, T., Rudnick, L., Stage, M. D., et al. 2010, ApJ, 725, 2038
Dwek, E., Galliano, F., & Jones, A. P. 2007, ApJ, 662, 927
Fesen, R. A., Hammell, M. C., Morse, J., et al. 2006, ApJ, 645, 283
Foster, A. R., Ji, L., Smith, R. K., & Brickhouse, N. S. 2012, ApJ, 756, 128
Gehrz, R. 1989, in IAU Symp. 135, Interstellar Dust, ed. L. J. Allamandola & A. G. G. M. Tielens (Cambridge: Cambridge Univ. Press), 445
Hwang, U., & Laming, J. M. 2003, ApJ, 597, 362
Hwang, U., & Laming, J. M. 2009, ApJ, 703, 883
Hwang, U., & Laming, J. M. 2012, ApJ, 746, 130
Hwang, U., Szymkowiak, A. E., Petre, R., & Holt, S. S. 2001, ApJL, 560, L175
Kirchschlager, F., Barlow, M. J., & Schmidt, F. D. 2020, ApJ, 893, 70
Kirchschlager, F., Schmidt, F. D., Barlow, M. J., et al. 2019, MNRAS, 489, 4465
Laming, J. M., & Hwang, U. 2003, ApJ, 597, 347
Mathis, J. S., Rumpl, W., & Nordsieck, K. H. 1977, ApJ, 217, 425
Micelotta, E. R., Dwek, E., & Slavin, J. D. 2016, A&A, 590, A65
Milisavljevic, D., & Fesen, R. A. 2013, ApJ, 772, 134
Nath, B. B., Laskar, T., & Shull, J. M. 2008, ApJ, 682, 1055
Niculescu-Duvaz, M., Barlow, M. J., Bevan, A., Milisavljevic, D., & De Looze, I. 2021, MNRAS, 504, 2133
Nobukawa, K. K., Hirayama, A., Shimaguchi, A., et al. 2019, PASJ, 71, 115
Nozawa, T., Kozasa, T., & Habe, A. 2006, ApJ, 648, 435
Nozawa, T., Kozasa, T., Umeda, H., Maeda, K., & Nomoto, K. 2003, ApJ, 598, 785
Orlando, S., Wongwathanarat, A., Janka, H. T., et al. 2022, A&A, 666, A2
Pei, Y. C., Fall, S. M., & Bechtold, J. 1991, ApJ, 378, 6
Priestley, F. D., Arias, M., Barlow, M. J., & De Looze, I. 2022, MNRAS, 509, 3163
Priestley, F. D., Barlow, M. J., & De Looze, I. 2019, MNRAS, 485, 440
Rho, J., Kozasa, T., Reach, W. T., et al. 2008, ApJ, 673, 271
Rho, J., Wallstrom, S., Muller, S., et al. 2019, arXiv:1906.02380
Rutherford, J., Dewey, D., Figueroa-Feliciano, E., et al. 2013, ApJ, 769, 64
Saji, S., Matsumoto, H., Nobukawa, M., et al. 2018, PASJ, 70, 23
Schneider, R., Ferrara, A., & Salvaterra, R. 2004, MNRAS, 351, 1379
Siegel, J., Dwarkadas, V. V., Frank, K. A., & Burrows, D. N. 2021, ApJ, 922, 67
Slavin, J. D., Dwek, E., Mac Low, M.-M., & Hill, A. S. 2020, ApJ, 902, 135
Smith, R. K., Brickhouse, N. S., Liedahl, D. A., & Raymond, J. C. 2001, ApJL, 556, L91
Tatischeff, V., Decourchelle, A., & Maurin, G. 2012, A&A, 546, A88
Wilms, J., Allen, A., & McCray, R. 2000, ApJ, 542, 914
Yamaguchi, H., Badenes, C., Petre, R., et al. 2014a, ApJL, 785, L27
Yamaguchi, H., Eriksen, K. A., Badenes, C., et al. 2014b, ApJ, 780, 136
Zhou, P., Li, J.-T., Zhang, Z.-Y., et al. 2018, ApJ, 865, 6